Title

Assessment of higher-order singular value decomposition denoising methods on dynamic hyperpolarized [1-13C]pyruvate MRI data from patients with glioma

Authors

Vaziri, Sana
Autry, Adam W
Lafontaine, Marisa
et al.

Publication Date

2022

DOI

10.1016/j.nicl.2022.103155

NeuroImage: Clinical 36 (2022) 103155

Contents lists available at ScienceDirect

NeuroImage: Clinical

journal homepage: www.elsevier.com/locate/ynicl

Assessment of higher-order singular value decomposition denoising methods on dynamic hyperpolarized [1-^{13}C]pyruvate MRI data from patients with glioma

Sana Vaziri [a], Adam W. Autry [a], Marisa Lafontaine [a], Yaewon Kim [a], Jeremy W. Gordon [a], Hsin-Yu Chen [a], Jasmine Y. Hu [a], Janine M. Lupo [a], Susan M. Chang [b], Jennifer L. Clarke [b], Javier E. Villanueva-Meyer [a,b], Nancy Ann Oberheim Bush [b], Duan Xu [a], Peder E.Z. Larson [a], Daniel B. Vigneron [a], Yan Li [a,*]

[a] Department of Radiology and Biomedical Imaging, University of California San Francisco, San Francisco, CA, United States
[b] Department of Neurological Surgery, University of California San Francisco, San Francisco, CA, United States

ARTICLE INFO

Keywords:
Hyperpolarized
Carbon-13
Denoising
Signal-to-noise ratio
Glioma
Higher-order singular value decomposition

ABSTRACT

Background: Real-time metabolic conversion of intravenously-injected hyperpolarized [1-^{13}C]pyruvate to [1-^{13}C]lactate and [^{13}C]bicarbonate in the brain can be measured using dynamic hyperpolarized carbon-13 (HP-^{13}C) MRI. However, voxel-wise evaluation of metabolism in patients with glioma is challenged by the limited signal-to-noise ratio (SNR) of downstream ^{13}C metabolites, especially within lesions. The purpose of this study was to evaluate the ability of higher-order singular value decomposition (HOSVD) denoising methods to enhance dynamic HP [1-^{13}C]pyruvate MRI data acquired from patients with glioma.

Methods: Dynamic HP-^{13}C MRI were acquired from 14 patients with glioma. The effects of two HOSVD denoising techniques, tensor rank truncation-image enhancement (TRI) and global–local HOSVD (GL-HOSVD), on the SNR and kinetic modeling were analyzed in [1-^{13}C]lactate data with simulated noise that matched the levels of [^{13}C]bicarbonate signals. Both methods were then evaluated in patient data based on their ability to improve [1-^{13}C]pyruvate, [1-^{13}C]lactate and [^{13}C]bicarbonate SNR. The effects of denoising on voxel-wise kinetic modeling of k_{PL} and k_{PB} was also evaluated. The number of voxels with reliable kinetic modeling of pyruvate-to-lactate (k_{PL}) and pyruvate-to-bicarbonate (k_{PB}) conversion rates within regions of interest (ROIs) before and after denoising was then compared.

Results: Both denoising methods improved metabolite SNR and regional signal coverage. In patient data, the average increase in peak dynamic metabolite SNR was 2-fold using TRI and 4–5 folds using GL-HOSVD denoising compared to acquired data. Denoising reduced k_{PL} modeling errors from a native average of 23% to 16% (TRI) and 15% (GL-HOSVD); and k_{PB} error from 42% to 34% (TRI) and 37% (GL-HOSVD) (values were averaged voxelwise over all datasets). In contrast-enhancing lesions, the average number of voxels demonstrating within-tolerance k_{PL} modeling error relative to the total voxels increased from 48% in the original data to 84% (TRI) and 90% (GL-HOSVD), while the number of voxels showing within-tolerance k_{PB} modeling error increased from 0% to 15% (TRI) and 8% (GL-HOSVD).

Conclusion: Post-processing denoising methods significantly improved the SNR of dynamic HP-^{13}C imaging data, resulting in a greater number of voxels satisfying minimum SNR criteria and maximum kinetic modeling errors in tumor lesions. This enhancement can aid in the voxel-wise analysis of HP-^{13}C data and thereby improve monitoring of metabolic changes in patients with glioma following treatment.

Abbreviations: SNR, signal-to-noise ratio; HP, hyperpolarized; HP-^{13}C, hyperpolarized carbon-13; HOSVD, higher-order singular value decomposition; TRI, tensor rank truncation-image enhancement; GL-HOSVD, global-local HOSVD; ROI, region of interest; LDH, lactate dehydrogenase; PDH, pyruvate dehydrogenase; QC, quality control; CEL, contrast-enhancing lesion; NEL, non-enhancing lesion; NAWM, normal appearing white matter; aSNR, apparent SNR; AUC, area-under-the-dynamic-curve; MSE, mean squared error.

* Corresponding author at: Department of Radiology and Biomedical Imaging, University of California San Francisco, 185 Berry Street, Ste 350, San Francisco, CA 94107, United States.

E-mail address: yan.li@ucsf.edu (Y. Li).

https://doi.org/10.1016/j.nicl.2022.103155
Received 17 May 2022; Received in revised form 12 August 2022; Accepted 13 August 2022
Available online 17 August 2022

1. Introduction

Dynamic hyperpolarized carbon-13 (HP-^{13}C) MR metabolic imaging is able to non-invasively capture real-time metabolism after injecting a pre-polarized ^{13}C-enriched probe (Ardenkjaer-Larsen et al., 2003). The most commonly used probe, HP [1-^{13}C]pyruvate, has been extensively evaluated in several human brain studies (Autry et al., 2020b; Grist et al., 2019; Lee et al., 2021a; Lee et al., 2020; Li et al., 2021; Miloushev et al., 2018; Park et al., 2018). The fundamental rationale for its use in brain tumors is the Warburg effect (Golman et al., 2006; Warburg, 1956), which describes the upregulation of glycolytic metabolism by way of increased lactate dehydrogenase (LDH) expression, with the simultaneous downregulation of oxidative phosphorylation (Schroeder et al., 2009) by way of decreased pyruvate dehydrogenase (PDH) in cancers. Previous studies characterizing brain tumors have shown increased conversion from [1-^{13}C]pyruvate to [1-^{13}C]lactate and decreased conversion from [1-^{13}C]pyruvate to [^{13}C]bicarbonate in progressive tumor compared to normal-appearing brain tissue (Autry et al., 2020a; Autry et al., 2020b; Park et al., 2018). The relatively low [^{13}C]bicarbonate signal, particularly in tumors due to metabolic reprogramming, has limited the ability to study oxidative phosphorylation using pyruvate-to-bicarbonate flux modeling (Autry et al., 2020b). In normal-appearing white matter (NAWM) voxels, the signal-to-noise ratio (SNR) of [^{13}C]bicarbonate data can be as much as 3-fold lower than that of [1-^{13}C]lactate (Autry et al., 2020b; Grist et al., 2019), which may hinder voxel-wise metabolite analysis for other applications (Grist et al., 2020).

A unique challenge associated with HP-^{13}C acquisitions lies in the irreversible and rapid decay of the hyperpolarized signal, which translates into limited SNR for measured metabolites following the injection of the tracer. Advances in HP-^{13}C acquisitions include the optimization of quality control (QC) steps to reduce the time-to-injection (Autry et al., 2020b; Li et al., 2021), using multichannel receiver coils (Autry et al., 2019; Sanchez-Heredia et al., 2020), and development of fast (Gordon et al., 2021) and variable resolution acquisitions for metabolites with different SNRs (Gordon et al., 2020). These advances have provided reliable enhancements for evaluating the human brain.

Post-processing denoising offers another avenue for improving the SNR of HP-^{13}C data after data acquisition. A breadth of higher-order singular value decomposition (HOSVD) techniques (De Lathauwer et al., 2000; Rajwade et al., 2013) that can produce up to a 10-fold increase in apparent SNR and have been applied to denoise MRI data (Brender et al., 2019; Lee et al., 2021b; Zhang et al., 2017; Zhang et al., 2015). HOSVD denoising methods rely on underlying assumptions of sparsity within the multidimensional data along with the presence of random, Gaussian-distributed noise. Under these conditions, noise reduction can be achieved via truncation of the HOSVD core tensor. Tensor decomposition methods, such as tensor rank truncation-image enhancement (TRI) (Chen et al., 2020), treat the data as a single tensor of spatial and temporal dimensions for denoising and have been applied to HP-^{13}C MR spectroscopic imaging (MRSI). A patch-based approach, global–local HOSVD (GL-HOSVD), applies a global HOSVD pre-filtering step before grouping similar data patches together and applying a local HOSVD denoising on each patch (Zhang et al., 2017). It has been reported that GL-HOSVD denoising increased the SNR of HP-^{13}C MRI data acquired from healthy brain volunteers (Kim et al., 2021).

The purpose of this study was to evaluate the ability of the denoising techniques TRI and GL-HOSVD to recover the signals obscured by noise from dynamic HP-^{13}C MRI of patients with glioma. Simulated low-SNR dynamic metabolite images derived from data acquired from patients were first denoised and compared to the acquired signals. Voxel-wise SNR improvements and the number of voxels with reliable kinetic modeling for [1-^{13}C]pyruvate, [1-^{13}C]lactate, and [^{13}C]bicarbonate were then evaluated within the anatomic lesions and normal-appearing brain.

2. Methods

2.1. Patient population and treatments

A total of 14 patients with adult-type grade 4 diffuse gliomas at different disease status (9 recurrent, 5 newly diagnosed) were involved in this study. Most patients had received a combination of different therapies. The characteristics of the studied patient population are summarized in Table 1. Each patient was given written informed consent in accordance with the University of California San Francisco IRB procedures.

2.2. Imaging protocol

All MR studies were performed using a dual-tuned ^{13}C volume transmit/24-channel receiver and ^{1}H 8-channel receiver head coil (Rapid Biomedical, Germany) on a 3 T scanner (GE Healthcare, Waukesha, WI). The standard-of-care anatomic imaging (Ellingson et al., 2015) consisted of 3D pre- and post-contrast T1-weighted inversion recovery-prepared spoiled gradient echo (IRSPGR) images (repetition time [TR]/echo time [TE]/inversion time [TI] = 8/3/400 ms, slice thickness = 1.5 mm, field of view [FOV] = 25.6 × 25.6 cm, matrix = 256 × 256) and T2-weighted fluid attenuated inversion recovery (FLAIR) images (TR/TE/TI = 6250/138/1702 ms, slice thickness = 1.5 mm, FOV = 25.6 × 25.6 cm, matrix = 256 × 256).

The procedures of obtaining HP [1-^{13}C]pyruvate MRI included

Table 1
Clinical patient summary.

No.	Age	Diagnosis	Disease status at imaging	Treatment Received	Subsequent clinical status
1	39	Astrocytoma, IDH-mutant, grade 4	Recurrent	Sx, RT, TMZ, bevacizumab	Stable
2	55	Glioblastoma, IDH-wildtype	Newly diagnosed	Sx, RT, TMZ	Stable
3	62	Glioblastoma, IDH-wildtype	Recurrent	Sx, RT, TMZ, DCvax Oliparib, everolimus, CCNU, bevacizumab	Progressed
4	70	Glioblastoma, IDH-wildtype	Recurrent	Sx, RT, TMZ, CCNU, Afatinib	Stable
5	63	Glioblastoma, IDH-wildtype	Recurrent	Sx, RT, TMZ	Stable
6	55	Glioblastoma, IDH-wildtype	Recurrent	Sx, RT, TMZ, CCNU, Trametinib, Everolimus	Progressed
7	51	Glioblastoma, IDH-wildtype	Recurrent	Sx, RT, TMZ, DCVax, Toca5FC, bevacizumab	Stable
8	58	Glioblastoma, IDH-wildtype	Newly diagnosed	RT, TMZ, Optune, CCNU, Afatinib, Abecliclab	Stable
9	44	Glioblastoma, IDH-wildtype	Recurrent	Sx, RT, TMZ	Stable
10	44	Glioblastoma, IDH-wildtype	Newly diagnosed	Sx, RT, TMZ, BGB-290	Stable
11	45	Glioblastoma, IDH-wildtype	Recurrent	Sx, Nivolumab, Poliovirus	Stable
12	63	Glioblastoma, IDH-wildtype	Recurrent	Sx, RT, TMZ	Stable
13	58	Glioblastoma, IDH-wildtype	Newly diagnosed	None	NA
14	55	Glioblastoma, IDH-wildtype	Newly diagnosed	None	NA

Sx = surgery; RT = radiation therapy; TMZ = temozolomide; CCNU = lomustine; DCVax = dendritic cell vaccine; Toca5fc = 5-flucytosine; BGB-290 = pamiparib.

sample preparation, hyperpolarization using the clinical SPINlab system (General Electric, Niskayuna, NY) and QC prior to injection (Autry et al., 2020b; Li et al., 2021; Park et al., 2018). The median and range values of QC and injection parameters were as follows: polarization = 38.3 [21.4, 46.4] %, pyruvate concentration = 232 [194, 259] (mM), pH = 7.8 [7.4, 8.2], and temperature = 32.0 [29.7, 34.3] °C, and injected pyruvate volume = 33 [24, 40] mL (values = median [min, max]). After on-site pharmacist approval, HP [1-^{13}C]pyruvate was injected intravenously at a dosage of 0.43 mL/kg followed by 20 mL saline (Autry et al., 2020b). Median and range of time-to-injection were = 50 [46, 72] seconds (median [min, max]). The noise-only data was acquired separately prior to the injection.

The frequency reference for [1-^{13}C]pyruvate acquisition was set using the *in vivo* center frequency of water from a ^{1}H scan together with a conversion factor between ^{1}H/^{13}C gyromagnetic ratios: $f_{pyruvate} = f_{water}$ x 0.2514918899. The dynamic HP-^{13}C scan began 5 s after the end of injection using a frequency-specific multislice echo planar imaging (EPI) sequence (TR/TE = 62.5 ms/21.7 ms, 1032 μs echo-spacing, ±10 kHz BW; 3 frequencies, [1-^{13}C]pyruvate, [1-^{13}C]lactate, [^{13}C]bicarbonate flip angles = 20°, 30°, 30°; FOV = 24.0 × 24.0 cm; 1.5 cm isotropic spatial resolution, 8 slices; 20 timepoints, 3 s temporal resolution; 60 s total acquisition time) (Autry et al., 2020b; Gordon et al., 2019; Gordon et al., 2017).

2.3. ROI segmentation

All the ^{1}H images were aligned to the corresponding T1-weighted post-contrast images (Li et al., 2011). The masks of T2 hyperintense lesions were segmented on FLAIR images while contrast-enhancing lesions (CEL) were defined from the post-contrast T1 images using 3D Slicer (https://www.slicer.org). Segmentation of white matter was performed on the T1-weighted pre-contrast images using in-house tools (Li et al., 2011; Zhang et al., 2001), and refined by excluding the cortex segmented by the automated anatomical labeling atlas 3 (Rolls et al., 2020) using nonlinear registration (FMRIB Software Library, fsl.fmrib.ox.ac.uk/fsl/fslwiki/FSL). All masks were down-sampled to the spatial resolution of ^{13}C data. Regions of interest (ROIs) were defined at HP-^{13}C resolution and included CEL (voxels comprised of > 20 % contrast-enhancing disease), non-enhancing lesion (NEL; non-enhancing voxels comprised of > 40 % T2 lesion), and normal appearing white matter (NAWM; non-T2 lesion voxels comprised of > 40 % white matter).

2.4. Post-processing of dynamic ^{13}C data

Raw dynamic ^{13}C *EPI* data from the 24-channel coil were first corrected for Nyquist ghosting artifacts using an exhaustive search (Wang et al., 2018). Prewhitening to reduce the effects of coil coupling was performed by determining the decorrelation matrix from noise data without HP substrate using Cholesky decomposition (Pruessmann et al., 2001) and then dividing the HP data by this matrix. Coil combination was performed using complex weights from pyruvate data (Zhu et al., 2019). Area-under-the-dynamic-curve (AUC) images were calculated for each metabolite by taking the temporal sum of dynamic images. Voxel-wise phase correction was performed separately for each metabolite by estimating the phase from complex AUC images (Crane et al., 2021).

2.5. Metabolic parameters derived from dynamic ^{13}C data

Noise levels for the dynamic data of each metabolite were estimated using the standard deviation of background voxels. Noise levels for the AUC images were estimated by dividing the estimated dynamic noise levels by the square root of the number of time points acquired. Peak dynamic SNR was defined as the maximum dynamic intensity divided by the dynamic noise level. Voxel-wise apparent SNR (aSNR) maps were calculated by dividing phase corrected AUC images by the AUC noise level. SNR masks were created to filter out voxels with aSNR < 5, as these were deemed unreliable.

Voxel-wise apparent rate constants for pyruvate-to-lactate (k_{PL}) and pyruvate-to-bicarbonate (k_{PB}) were quantified from dynamic HP-^{13}C data using an input-less kinetic model (Autry et al., 2020b; Larson et al., 2018; Mammoli et al., 2020). Modeling fit errors were defined as the 95 % confidence interval of the fit (Mammoli et al., 2020). Modeling error masks for k_{PL} and k_{PB} maps were created to filter out voxels with errors >30 % and 50 % of the estimated value, respectively. Signal coverages, or quantifiable regions, were calculated as a percentage of total voxels within each ROI after filtering by SNR mask ($\%N_{pyruvate}$, $\%N_{lactate}$, $\%N_{bicarbonate}$) or modeling error masks ($\%N_{kPL}$, $\%N_{kPB}$). Ratios of lactate-to-pyruvate, bicarbonate-to-pyruvate, and bicarbonate-to-lactate were calculated from AUC maps after applying SNR masks.

2.6. Data analysis

2.6.1. Denoising parameters

All denoising was performed on the real part of phased dynamic metabolite data. TRI denoising was applied to each metabolite data separately (Chen et al., 2020). The input tensor was the entire dynamic metabolite volume of size 16 × 16 × 8 × 20 (3 spatial dimensions, 1 temporal dimension). The tensor rank was set to 10 × 10 × 8 in the spatial dimensions and 4 in the temporal dimension. This value was selected after optimizing for lowest denoised lactate signal mean squared error (MSE) and then increasing the rank in the in-plane spatial dimension based on the smoothing artifacts, size of the imaged brain, and the multi-linear singular values of the input tensor in each dimension. GL-HOSVD denoising (https://github.com/XinyuanZhang719/gl-hosvd) was applied on a slice-by-slice basis to each dynamic metabolite image, as previously described (Kim et al., 2021). The input tensor was of size 16 × 16 × 20 (2 spatial, 1 temporal dimension), the patch size was 4 × 4, and the search window size for finding similar patches was 6 × 6. After optimizing for lowest denoised lactate signal MSE, the parameter k_{global} was set to 0.4, and k_{local} was set to be between 0.6 and 0.8.

2.6.2. Evaluation of denoising methods using simulations

Zero-mean Gaussian noise was simulated and added to acquired phased dynamic [1- ^{13}C]lactate data to match the SNR level of [^{13}C]bicarbonate signals. The resulting signal is referred to as the noise-added data and was then denoised using TRI and GL-HOSVD (hereafter referred to as the noise-added + TRI and noise-added + GL-HOSVD data, respectively). Denoised signals were compared against the acquired signal, although it should be noted that the acquired signal is not noise-free. For each patient dataset, noise level, peak dynamic SNR, SNR masks, k_{PL} values, and k_{PL} modeling errors were calculated for noise-added, noise-added + TRI, and noise-added + GL-HOSVD data. MSE values were computed against the ground truth for dynamic traces and k_{PL} maps restricted to each ROI. Dice scores were calculated comparing SNR masks and modeling error masks to their acquired data counterparts. Two-sample t-tests with a significance level of p-value < 0.05 were performed to compare two denoising methods and determine the significance of SNR and coverage improvements of denoising across all datasets.

2.6.3. Evaluation of denoising on patient data

For each patient dataset, the acquired [1-^{13}C]pyruvate, [1-^{13}C]lactate, and [^{13}C]bicarbonate signals were denoised using TRI and GL-HOSVD. The peak dynamic SNR values, SNR masks, and voxel-wise k_{PL} and k_{PB} maps were calculated using the acquired data, TRI denoised, and GL-HOSVD denoised data. $\%N_{pyruvate}$, $\%N_{lactate}$, $\%N_{bicarbonate}$, $\%N_{kPL}$, and $\%N_{kPB}$ were also computed within each ROI for the acquired and denoised data. Two-sample t-tests with a significance level of p-value < 0.05 was performed to compare voxel-wise values between acquired and denoised data, and between two denoising methods within each ROI (NAWM, NEL, CEL).

3. Results

3.1. Denoising effects on simulated data SNR

In the acquired data, peak dynamic SNRs were 22.7 ± 14.8 [6.7, 59.0] (mean ± standard deviation [min, max], all 14 datasets) for lactate and 8.0 ± 4.1 [4.1, 18.0] for bicarbonate. Using a Gaussian distribution with standard deviation set to 1.25, the peak dynamic SNRs for the noise-added lactate signal were 6.7 ± 2.3 [4.0, 10.6]. The noise-added datasets better matched SNR levels of the acquired bicarbonate data (p-value > 0.05). After denoising, the SNRs were increased to 22.7 ± 14.8 [6.7, 59.1] (noise-added + TRI) and 30.0 ± 16.1 [8.8, 64.7] (noise-added + GL-HOSVD). The noise levels, as estimated from the background voxels of dynamic datasets, decreased significantly after denoising (p-value < 0.001), with the standard deviation of the background voxels being 1.5 ± 0.7 [1.2, 3.7] before denoising and 0.5 ± 0.3 [0.3, 1.6] (TRI) and 0.3 ± 0.3 [0.1, 1.3] (GL-HOSVD) following denoising. Denoising reduced noise levels below that of the acquired lactate signal, 0.5 ± 0.9 [0.1, 3.8]. The two methods performed comparably in terms of noise reduction (p-value > 0.05). An example of the acquired lactate signal, noise-added lactate, denoised, and acquired bicarbonate metabolite data is shown in Fig. 1.

An example of SNR masks before and after denoising compared to the mask of the acquired signal is shown in Fig. 2A. Fig. 2B – 2D demonstrate $\%N_{lactate}$, dice scores, and MSE values from all the subjects within each ROI. After applying denoising, $\%N_{lactate}$ within the entire brain was significantly increased compared to the noise-added signals (TRI: p-value < 0.0001, GL-HOSVD: p-value < 0.0001) and comparable

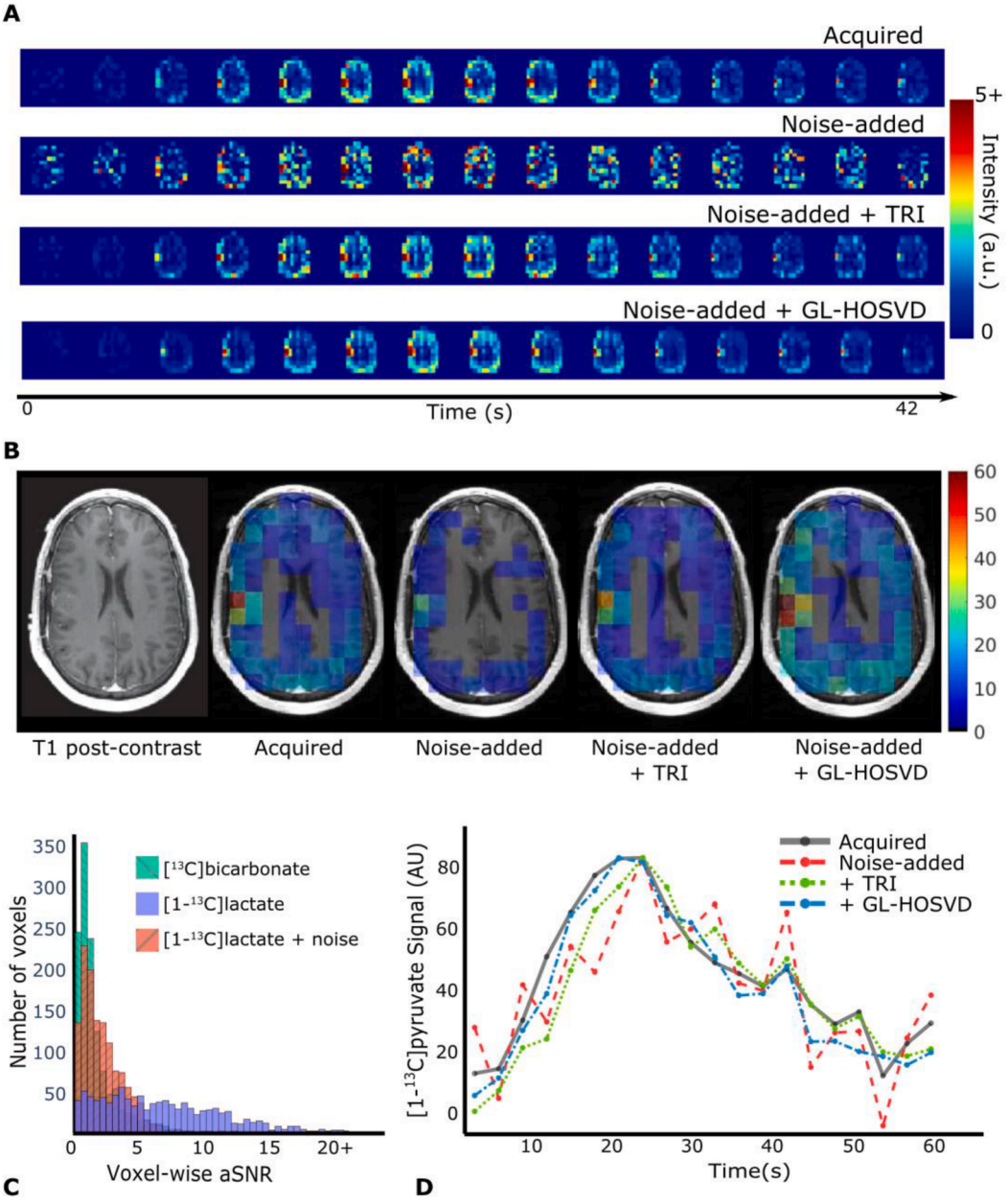

Fig. 1. Example of denoising lactate signal with additional simulated noise. HP-^{13}C *EPI* data were acquired from a patient with a newly-diagnosed glioblastoma (Patient 14). Gaussian noise was added to the acquired lactate signal to match the SNR of the acquired bicarbonate signal. (A) Acquired, noise-added, noise-added + TRI, and noise-added + GL-HOSVD [1-^{13}C]lactate dynamic images from one slice. (B) Voxel-wise aSNR maps (filtered by SNR masks) overlaid on axial T1 post-Gd images. (C) Histograms of voxel-wise aSNR for the acquired lactate (purple), noise-added lactate (red), and acquired bicarbonate (green) signals. (D) Dynamic traces averaged over all the voxels within the NAWM for each lactate signal.

to the acquired signal for both methods (p-value > 0.05). Dice scores of SNR masks within the brain increased from 0.2 ± 0.3 [0.0, 0.9] (noise-added) to 0.9 ± 0.2 [0.3, 1] (noise-added + TRI) and 0.9 ± 0.1 [0.6, 1.0] (noise-added + GL-HOSVD), respectively. MSE values for dynamic traces within the brain were lowered from 1.9 ± 1.2 [1.5, 6.4] (noise-added) to 1.1 ± 2.6 [0.2, 10.3] (noise-added + TRI) and 0.7 ± 1.7 [0.1, 7.0] (noise-added + GL-HOSVD), respectively. Compared to TRI, GL-HOSVD denoising recovered the acquired dynamic lactate signal values with better accuracy within the brain for each ROI; however, the performance of the two was comparable over the entire brain (comparing noise-added + TRI and noise-added + GL-HOSVD dice scores and MSE values, p-values > 0.05).

3.2. Denoising effects on kinetic modeling in simulated data

An example histogram of k_{PL} modeling error for data from Patient 14 is shown in Fig. 3A. The noise-added signal produces higher errors when compared to the acquired signal and subsequent denoising shifts the distribution of errors back towards that of the acquired distribution.

Across all patients, the coverage $\%N_{kPL}$, dice scores, and MSE values of k_{PL} within each ROI are shown in Fig. 3B-3D. Following denoising, $\%N_{kPL}$ within the brain increased significantly compared to the noise-added signals (p-values < 0.005 for TRI, GL-HOSVD) while being comparable to the acquired coverages (p-value > 0.05 for TRI, GL-HOSVD). Dice scores of k_{PL} modeling error masks within the brain increased significantly from 0.1 ± 0.2 [0, 0.8] (noise-added) to 0.6 ± 0.2 [0.2, 0.9] (noise-added + TRI, p-values < 0.0005) and 0.6 ± 0.3 [0.0, 1.0] (noise-added + GL-HOSVD, p-values < 0.0005). MSE values for k_{PL} values compared to acquired data k_{PL} within the brain were reduced from 1.2 ± 2.3 [0.8, 8.8] × 10^{-4} (noise-added) to 0.6 ± 0.9 [0.09, 3.4] × 10^{-4} (noise-added + TRI, p-value > 0.05) and 0.5 ± 0.8 [0.1, 3.3] × 10^{-4} (noise-added + GL-HOSVD, p-value > 0.05). Over the entire brain, the performances of the two were comparable (comparing noise-added + TRI and noise-added + GL-HOSVD dice scores and MSE values over the entire brain, p-value > 0.05). Across all patients, there was no significant difference in the mean k_{PL} values in NAWM voxels between any of the signals (acquired, noise-added, noise-added + TRI, and noise-added + GL-HOSVD; p-values > 0.05 between all pairs).

It should be noted that for datasets with low SNR, acquired data had both a limited SNR mask and k_{PL} error mask, making simulated denoising results difficult to assess. For example, the acquired data for Patient 6 exhibited a particularly low $\%N_{kPL}$ of 0.5 % (2 voxels in the brain) and the dice score is 0.0 for GL-HOSVD. In such a case, comparisons between acquired and noise-added + denoised data were unreliable as the acquired data is not necessarily the ground truth. This is particularly true in the limited voxels of small lesion and is demonstrated by the large confidence intervals in Fig. 2(d) and 3(d).

3.3. Denoising effects on SNR for patient data

Denoising significantly reduced noise levels in all metabolites (p-value < 0.05 for acquired vs TRI and GL-HOSVD both). Comparing TRI denoised and GL-HOSVD denoised noise levels showed GL-HOSVD provided significantly lower noise compared to TRI (p-value < 0.05) for pyruvate and bicarbonate data (p-value > 0.05 for lactate signals). Fig. 4A shows the improvement in the peak dynamic SNR for each of the acquired metabolite signals following denoising for all datasets (ratio of peak dynamic SNR values following denoising to that of the acquired signal). GL-HOSVD provides significantly higher improvement in SNR for pyruvate and bicarbonate data compared to TRI (p-value < 0.0005; p-value > 0.05 for lactate data). Table 2 summarizes the improvement in peak dynamic SNRs within the whole brain for each metabolite (ratios of denoised SNRs to acquired SNRs). GL-HOSVD provided improvements up to a factor of 8 for [^{13}C]bicarbonate data, while TRI provided improvements up to a factor of 3. Fig. 4B-4D illustrate the $\%N_{pyruvate}$, $\%N_{lactate}$, $\%N_{bicarbonate}$ within each ROI for the acquired and denoised data. Although $\%N_{bicarbonate}$ was improved significantly within the brain (TRI, p-value < 0.05; GL-HOSVD, p-value < 0.005), the coverage remained limited within the CEL for all the patients. The two methods provide similar coverages for all metabolites across the entire brain (p-value > 0.05).

3.4. Denoising effects on kinetic modeling for patient data

An example of the k_{PL} and k_{PB} maps before and after applying GL-HOSVD denoising to all metabolite signals is shown in Fig. 5A. Although brain coverage of the k_{PB} map increased following denoising, the signal in the lesion remained low. This is indicative of a reduction in pyruvate-to-bicarbonate conversion in the lesion compared to the contralateral brain in this patient. The $\%N_{kPL}$, $\%N_{kPB}$, $\%N_{lactate\text{-}to\text{-}pyruvate}$ and $\%N_{bicarbonate\text{-}to\text{-}lactate}$ within each ROI over all patient datasets are shown in Fig. 5B-5E. Averaged over all datasets, the voxel-wise average masked k_{PL} modeling error decreased from 23 % (acquired) to 16 % (TRI) and 15 % (GL-HOSVD). Similarly, k_{PB} modeling errors decreased from 42 % (acquired) to 34 % (TRI) and 37 % (GL-HOSVD). In the CEL, $\%N_{kPL}$ increased from about 48 % (acquired) of the ROIs to 84 % (TRI) and 90 % (GL-HOSVD). As with the $\%N_{bicarbonate}$, the $\%N_{kPB}$ and $\%N_{bicarbonate\text{-}to\text{-}lactate}$ were not fully recovered in the CEL, with $\%N_{kPB}$ increasing from no coverage (0 %; acquired) to 15 % (TRI) and 8 % (GL-HOSVD) and $\%N_{bicarbonate\text{-}to\text{-}lactate}$ increasing from no coverage (acquired) to 17 % (TRI) and 21 % (GL-HOSVD). Both methods significantly increased coverage over the entire brain ($\%N_{kPL}$, $\%N_{kPB}$ $\%N_{pyruvate\text{-}to\text{-}}$

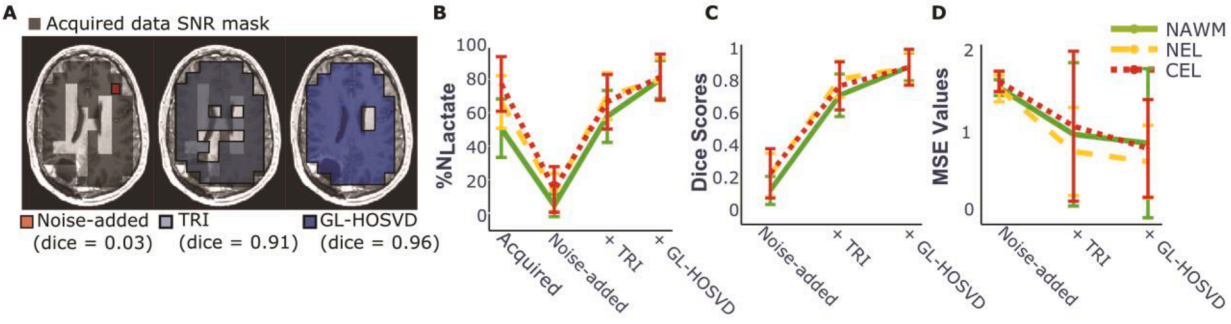

Fig. 2. Denoising effects on lactate signals with simulated noise. (A) Examples of lactate SNR masks (Patient 7). The SNR masks of noise-added (left, red overlay), noise-added + TRI (middle, light blue overlay), and noise-added + GL-HOSVD (right, dark blue overlay), are compared to the mask of the acquired data (indicated in each by the dark shaded voxels). Both TRI and GL-HOSVD denoising methods significantly improve the volume of SNR masks. Masks are overlaid on axial T1 post-Gd images with surgical cavity located at the right parietal lobe. (B)-(D) Denoising effects from all the patient datasets. The signal coverage ($\%N_{lactate}$), dice scores of SNR masks relative to acquired data mask, and voxel-wise dynamic lactate MSE values for voxels filtered by SNR mask are shown within each ROI for noise-added, noise-added + TRI, and noise-added + GL-HOSVD data. Values refer to mean and 95 % confidence intervals across all datasets. While both denoising methods recover many of the acquired voxels, the GL-HOSVD provides an advantage and produces higher dice scores and lower MSE values compared to TRI.

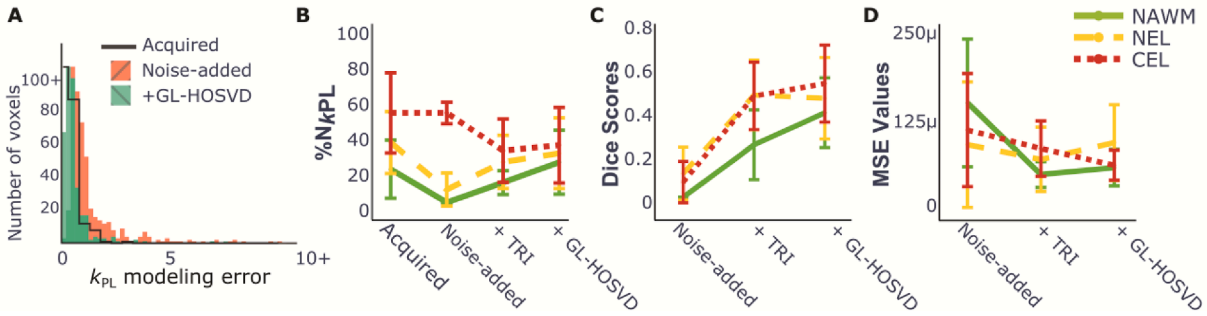

Fig. 3. Denoising effects on kinetic modeling of k_{PL} with simulated noise. (A) Example of k_{PL} modeling errors within the brain (Patient 14). The shift of the modeling error distribution for the noise-added signal (red) towards the acquired (black outline) after GL-HOSVD denoising (green). (B)-(D) Denoising effects from all the patient datasets. The %N$_{kPL}$, dice scores for error masks compared to the error mask of the acquired signal, and voxel-wise k_{PL} MSE values were plotted within each ROI for noise-added, noise-added + TRI, and noise-added + GL-HOSVD data. Values refer to mean and 95 % confidence intervals across all datasets. The %N$_{kPL}$ improved following denoising and are comparable to the acquired. The k_{PL}, accuracy compared to acquired data is, however, variable between datasets and, in particular, within smaller CEL and NEL.

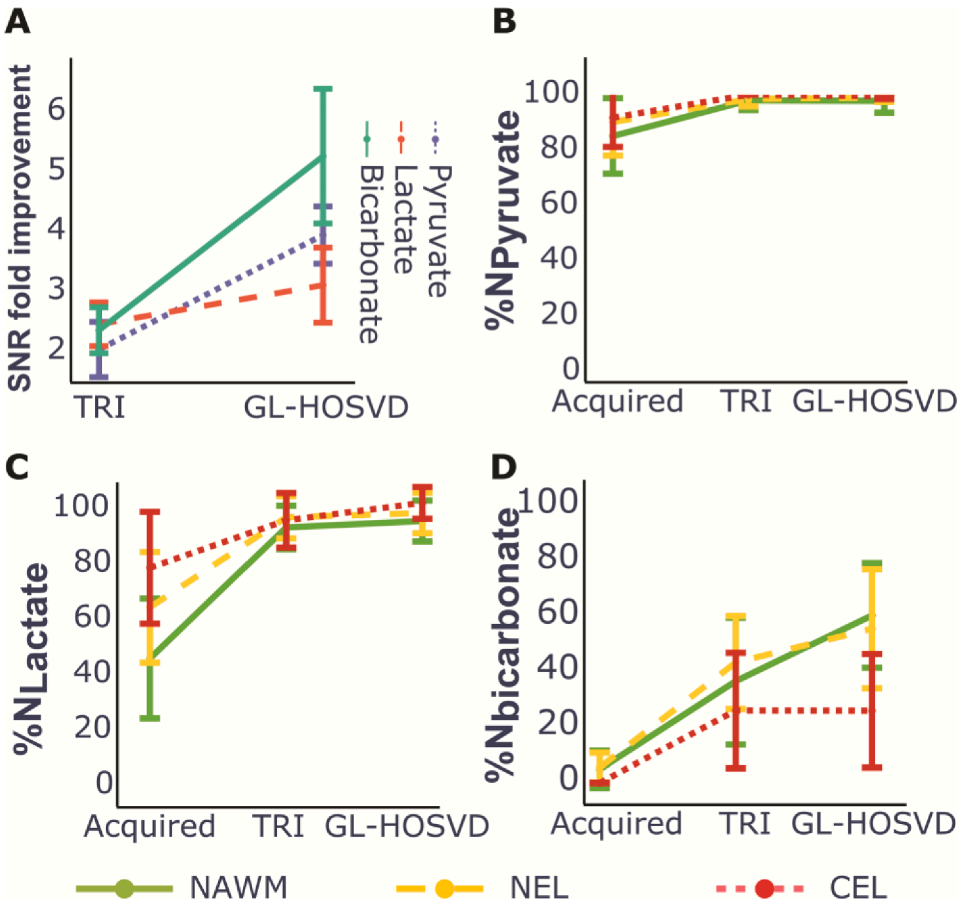

Fig. 4. Denoising effects on SNR and coverage in patient data. Peak dynamic SNR after denoising with TRI and GL-HOSVD were compared to the acquired signal (SNR fold improvement) (A). Metabolite coverages within each ROI for %N$_{pyruvate}$ (B), %N$_{lactate}$ (C), and %N$_{bicarbonate}$ (D) were calculated using acquired, TRI denoised, and GL-HOSVD denoised signals. Values refer to mean and 95% confidence intervals across all datasets. Both TRI and GL-HOSVD improved the SNRs and ROI coverages for [1-^{13}C]pyruvate, [1-^{13}C]lactate, and [^{13}C]bicarbonate signals. GL-HOSVD provided an advantage over TRI on the %N for [1-^{13}C]lactate and [^{13}C]bicarbonate signals.

Table 2
Peak denoised metabolite SNR fold improvement in patient data. Fold improvement to the peak dynamic SNRs following denoising was calculated for each metabolite relative to the acquired data. Values are mean ± standard deviation [min, max] over all 14 datasets.

	[1-^{13}C]pyruvate	[1-^{13}C]lactate	[^{13}C]bicarbonate
TRI	2.3 ± 0.9 [1.3, 4.0]	2.8 ± 1.1 [1.6, 5.7]	2.4 ± 0.8 [1.3, 3.7]
GL-HOSVD	3.9 ± 0.8 [2.7, 5.3]	3.1 ± 1.1 [1.9, 6.2]	5.1 ± 2.2 [1.1, 7.9]

$_{lactate}$, %N$_{bicarboante\text{-}to\text{-}lactate}$ p-values < 0.05, TRI, GL-HOSVD both). The two methods performed comparably in terms of number of voxels recovered over the entire brain (p-values > 0.05 for all). Across all patients, the mean k_{PL} values in NAWM did not change significantly after denoising (TRI, p-value > 0.05; GL-HOSVD, p-value > 0.05). Comparison of mean modeled values are more challenging in lesions given limited number of voxels.

The patients recruited for this study were at various clinical stages and thus analysis between the ROIs was not performed across patients. Examples of GL-HOSVD denoised data from a patient acquired prior to receiving any treatment (Patient 14), a patient with recurrent stable disease (Patient 8), and a patient with recurrent progressive disease

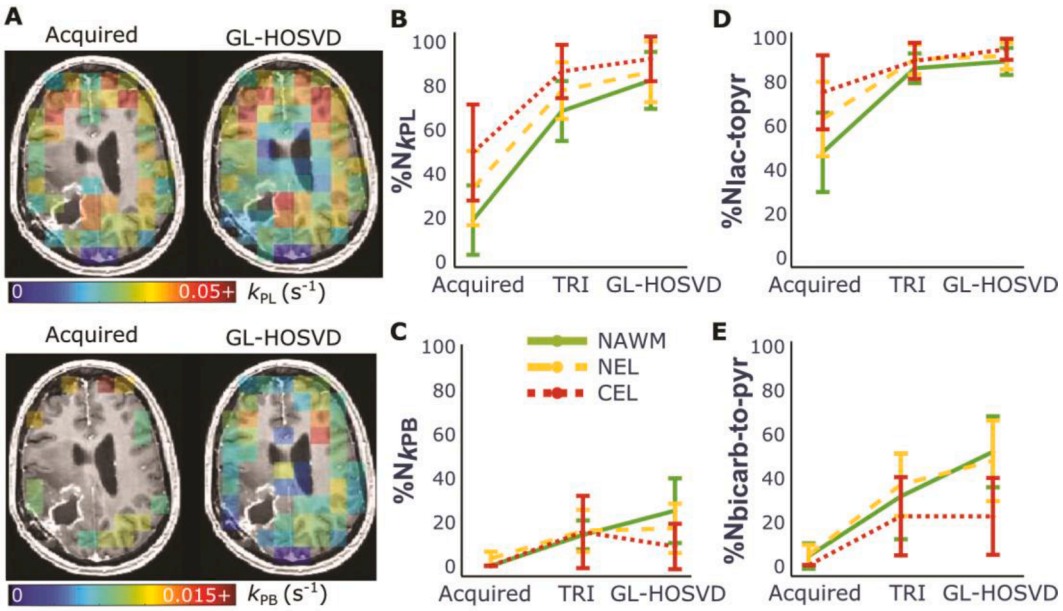

Fig. 5. Denoising effects on kinetic modeling coverage (patient data). (A) Examples of k_{PL} and k_{PB} maps filtered by modeling error masks overlaid on axial T1 post-Gd images before and after applying GL-HOSVD denoising (Patient 8). (B)-(E) $\%N_{kPL}$, $\%N_{kPB,}$ $\%N_{lactate\text{-}to\text{-}pyruvate}$ and $\%N_{bicarbonate\text{-}to\text{-}lactate}$ within each ROI calculated using acquired, TRI denoised, and GL-HOSVD denoised signals from all the patient datasets. Values refer to mean and 95% confidence intervals across all datasets. The k_{PL} coverages were improved after denoising.

(Patient 2) are illustrated in Figs. 6–8. All three patients had significant reductions in k_{PB} and bicarbonate-to-lactate within the NEL compared to the NAWM. Increased k_{PL} values were observed in the CEL of the recurrent patient with the progressive disease, while the $\%N_{bicarbonate}$ and $\%N_{kPB}$ values are limited in the CEL. In contrast, the bicarbonate signals are quantifiable within the CEL in the recurrent patient with stable disease.

4. Discussion

This study evaluated the ability of TRI and GL-HOSVD to improve the quantification of HP-^{13}C signals acquired from patients with glioma. Denoising ability was assessed using SNRs (peak dynamic SNRs and voxel-wise aSNRs) and kinetic modeling errors on patient datasets with and without additional simulated noises. While both methods improved metabolite SNR and coverages, GL-HOSVD provided an advantage over

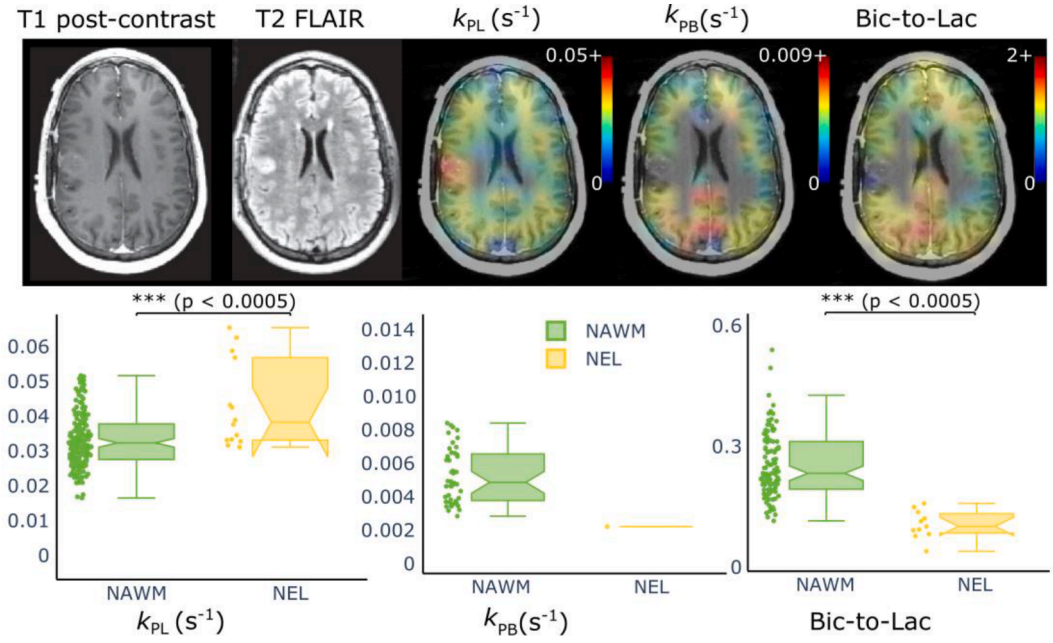

Fig. 6. Example of denoised data from a patient with newly diagnosed glioblastoma. A representative slice of ^{1}H images and HP-^{13}C *EPI* images (overlaid on the axial T1 post-Gd image and linearly interpolated in-plane to ^{1}H resolution) acquired from a patient with a newly diagnosed glioblastoma (Patient 8) are shown. Data was acquired prior to the patient receiving any treatment. The k_{PL}, $k_{PB,}$ and bicarbonate-to-lactate values within each ROI (NAWM, NEL, CEL) are shown in the boxplots following 2x in-plane interpolation of GL-HOSVD denoised metabolites signals. The k_{PL} values within the NEL were significantly higher compared to NAWM (p-value < 0.0005), while bicarbonate-to-lactate values were reduced significantly (p-value < 0.0005). k_{PB} coverage is low within the NEL.

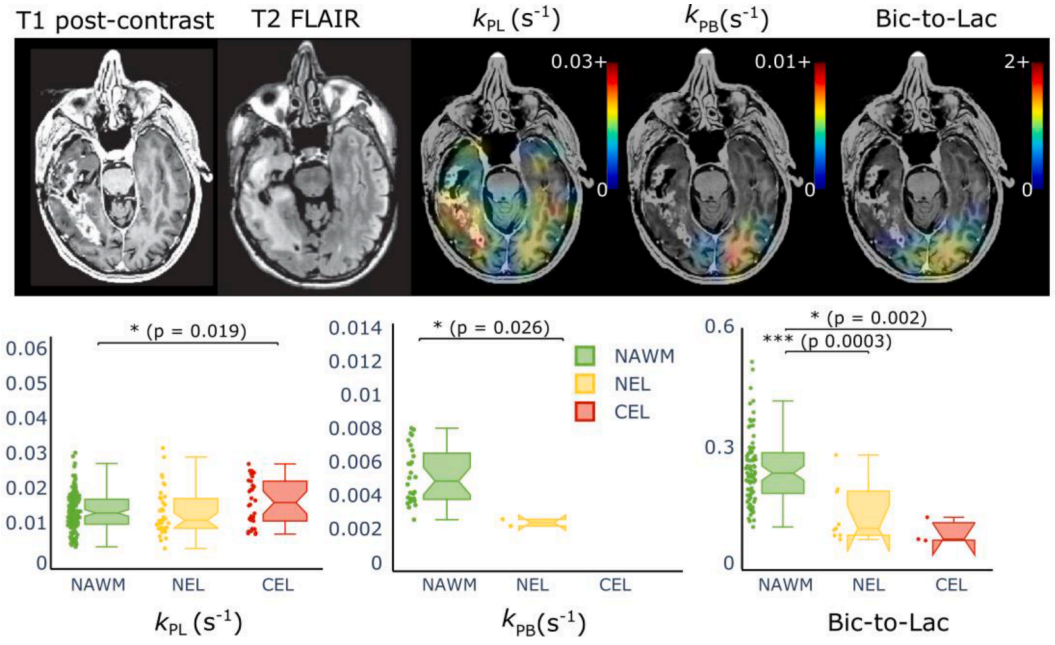

Fig. 7. Example of denoised data from a patient with recurrent, progressive disease. A representative slice of ^{1}H images and HP ^{13}C *EPI* (overlaid on the axial T1 post-Gd image and linearly interpolated in-plane to ^{1}H resolution) acquired from a patient with a recurrent glioblastoma are shown (Patient 2). Patient was scanned at the time of disease progression. The k_{PL}, $k_{PB,}$ and bicarbonate-to-lactate values within each ROI (NAWM, NEL, CEL) are shown in the boxplots following 2x in-plane interpolation of GL-HOSVD denoised metabolites signals. The k_{PL} values within the CEL were significantly higher compared to NAWM ($p = 0.019$), while k_{PB} was significantly reduced. k_{PB} ($p = 0.026$) and bicarbonate-to-lactate ($p = 0.0003$) within the NEL were also reduced compared to NAWM.

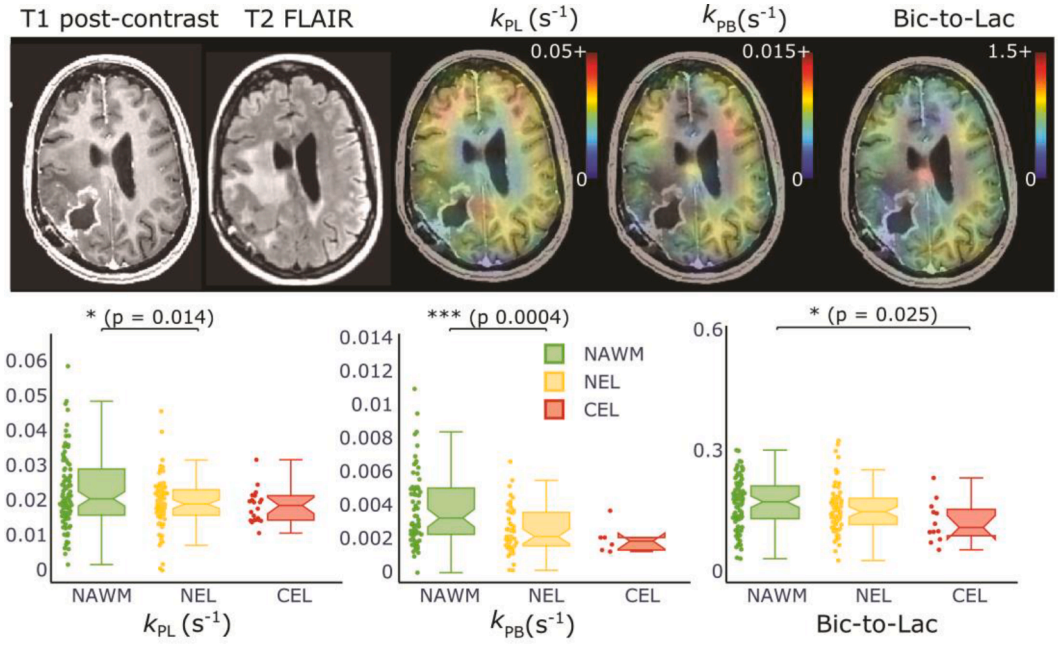

Fig. 8. Example of denoised data from a recurrent patient with stable disease. A representative slice of ^{1}H images and HP ^{13}C *EPI* images (overlaid on the axial T1 post-Gd image and linearly interpolated in-plane to ^{1}H resolution) acquired from a patient with a recurrent glioblastoma are shown (Patient 8). The k_{PL}, $k_{PB,}$ and bicarbonate-to-lactate values within each ROI (NAWM, NEL, CEL) are shown in the boxplots following 2x in-plane interpolation of GL-HOSVD denoised metabolites signals. No significant difference was found between the k_{PL} values within the CEL or NEL compared to NAWM in this patient, while k_{PB} within the NEL and bicarbonate-to-lactate within the CEL were reduced compared to NAWM ($p = 0.025$).

TRI on voxel-wise peak dynamic SNR, metabolite coverages, and k_{PL} and k_{PB} coverages in many cases.

Image denoising often poses a trade-off between SNR improvements and loss of spatial and temporal delineation. The denoising methods evaluated in this work rely on the inherent compressibility of images to remove noise components via HOSVD. TRI denoising uses a pre-selected rank and imposes a trade-off between SNR improvements and over-truncation of the HOSVD core matrix. The latter could result in blurring artifacts, requiring more attention for selecting the rank of the spatial dimensions. Given the high compressibility of HP-^{13}C MRI in the dynamic dimension, a small temporal rank was selected to provide more conservative noise removal that maintained voxel-wise differences,

which are critical in the analysis of aberrant metabolism. Although a fixed tensor rank was used, it is important to visually inspect results for artifacts and structural similarity between the original and denoised images. Inspection of the singular values of the core tensor can also help with rank selection. As with TRI, k_{global} and k_{local} parameters in GL-HOSVD, which affect the level of smoothing observed in the final images, may need to be adjusted after visually assessing smoothing artifacts. In this work, k_{global} and k_{local} were first optimized using the noise-added lactate datasets to produce the lowest dynamic lactate MSE. Smoothing artifacts in both the denoised dynamic images and denoised AUC images were found to be sensitive to higher k_{local} values. Thus, this parameter was reduced to ameliorate smoothing artifacts and accordingly produced conservative improvements in SNR.

One important prerequisite to using the HOSVD denoising methods is the presence of Gaussian noise. Thus, such methods may not be directly applicable to magnitude MR images that contain Rician noise (Gudbjartsson and Patz, 1995). As described previously (Kim et al., 2021), denoising was applied to the real part of phased dynamic images, which exhibited characteristics of Gaussian noise. Due to the lack of ground truth and benchmark data in evaluating denoising techniques for dynamic HP-^{13}C MRI patient datasets, we used voxel-wise modeling errors based on the least-squares confidence intervals to evaluate denoising performance on the ability to recover estimated k_{PL} and k_{PB} values. Given the model's assumption of Gaussian noise, these denoising methods are expected to reduce such fitting errors. However, kinetic modeling performed under assumptions of other noise characteristics may require more conservative noise removal to avoid introducing any modeling biases. A number of machine-learning based approaches have been introduced for denoising ^{1}H MRSI data (Hatami et al., 2018; Lam et al., 2020; Lei et al., 2021). These methods rely on high-quality datasets and are not currently applicable to HP-^{13}C studies. In the future, as more datasets become available, such techniques for signal enhancement may confer reliable improvements to dynamic HP-^{13}C data post-processing.

Of particular interest in this study was the signal enhancement achieved with respect to [^{13}C]bicarbonate in normal appearing brain tissue and tumor lesions. Because the real part of phase-corrected dynamic HP-^{13}C signals exhibit Gaussian noise (Kim et al., 2021), simulation experiments were performed by adding Gaussian noise to the acquired phased dynamic [1-^{13}C]lactate signal. The artificially reduced lactate SNR resulted in signal quality comparable to that of the acquired bicarbonate data. Because there is no inherently high-SNR bicarbonate data in patients, the noise-added lactate data served as a proxy to evaluate the performance of bicarbonate denoising. Using GL-HOSVD, the peak dynamic SNR of [^{13}C]bicarbonate signals in patient data were improved as much as 8-fold. Despite this boost in SNR, the number of voxels within the CEL with aSNR greater than 5 remained limited. Similarly, the number of voxels in the CEL with sufficiently low k_{PB} modeling error was few in each dataset. Given the ability of GL-HOSVD to recover lactate signal in the CEL when the data were artificially obscured by noise, these results support that known metabolic reprograming (Warburg effects) results in increased conversion of pyruvate to lactate rather than to bicarbonate in active tumor.

The increased coverage following GL-HOSVD denoising allowed for voxel-wise regional analysis of metabolic differences, although this was not the focus of the study. The 3 patients shown in Figs. 6–8 had a significant reduction in the conversion from pyruvate to bicarbonate within the NEL compared to NAWM. In addition, the patient with progressive disease (Fig. 7, Patient 2) exhibited significantly higher k_{PL} values within the CEL compared to NAWM, while this was not seen in the patient with clinically stable disease (Fig. 8). This is consistent with our previous findings in progressive patients (Autry et al., 2020a). Additionally, the bicarbonate signal was not quantifiable in the CEL of the recurrent patient with progressive disease, which may be indicative of a reduction in the conversion from pyruvate to bicarbonate in the active tumor. It is important to note, however, that treatment-induced changes may also contribute to observed metabolic differences. Further investigation of region-wide differences in HP-^{13}C parameters is needed in a larger set of patients to account for tumor heterogeneity, variations in treatment, and the different clinical stages at the time of the scan.

5. Conclusion

The ability of TRI and GL-HOSVD denoising methods to improve signal quality were evaluated on dynamic HP-^{13}C MRI data acquired from patients with glioma. Both methods improved the SNRs for acquired metabolite data as well as quantified k_{PL} and k_{PB} maps, with GL-HOSVD providing more of an increase in SNR than TRI. Although simulations show both post-processing HOSVD methods can recover artificially low-SNR dynamic metabolite images, the bicarbonate signal within the tumor lesion remains notably low after denoising, indicating increased pyruvate conversion to lactate through LDH and reduced PDH catalyzed conversion to CO_2/bicarbonate.

CRediT authorship contribution statement

Sana Vaziri: Conceptualization, Formal analysis, Methodology, Writing – original draft. **Adam W. Autry:** Conceptualization, Methodology, Writing – review & editing. **Marisa Lafontaine:** Writing – review & editing. **Yaewon Kim:** Methodology, Writing – review & editing. **Jeremy W. Gordon:** Conceptualization, Methodology, Writing – review & editing. **Hsin-Yu Chen:** Methodology, Writing – review & editing. **Jasmine Y. Hu:** Writing – review & editing. **Janine M. Lupo:** Conceptualization, Funding acquisition, Writing – review & editing. **Susan M. Chang:** Conceptualization, Funding acquisition, Writing – review & editing. **Jennifer L. Clarke:** Conceptualization, Funding acquisition, Writing – review & editing. **Javier E. Villanueva-Meyer:** Conceptualization, Writing – review & editing. **Nancy Ann Oberheim Bush:** Writing – review & editing. **Duan Xu:** Conceptualization, Funding acquisition, Writing – review & editing. **Peder E.Z. Larson:** Conceptualization, Methodology, Writing – review & editing. **Daniel B. Vigneron:** Conceptualization, Funding acquisition, Writing – review & editing. **Yan Li:** Conceptualization, Funding acquisition, Supervision, Writing – review & editing.

Declaration of Competing Interest

The authors declare that they have no known competing financial interests or personal relationships that could have appeared to influence the work reported in this paper.

Data availability

Data will be made available on request.

Acknowledgements

This project was supported by NIH T32 CA151022, R01 CA262630, P01 CA118816, P41EB013598, P50 CA097257, Department of Defense W81XWH2010292, and the Glioblastoma Precision Medicine Program.

References

Ardenkjaer-Larsen, J.H., Fridlund, B., Gram, A., Hansson, G., Hansson, L., Lerche, M.H., Servin, R., Thaning, M., Golman, K., 2003. Increase in signal-to-noise ratio of > 10,000 times in liquid-state NMR. Proc. Natl. Acad. Sci. USA 100, 10158–10163.

Autry, A.W., Gordon, J.W., Carvajal, L., Mareyam, A., Chen, H.-Y., Park, I., Mammoli, D., Vareth, M., Chang, S.M., Wald, L.L., Xu, D., Vigneron, D.B., Nelson, S.J., Li, Y., 2019. Comparison between 8- and 32-channel phased-array receive coils for in vivo hyperpolarized (13) C imaging of the human brain. Magn. Reson. Med. 82 (2), 833–841.

Autry, A., Gordon, J., LaFontaine, M., Chen, H.Y., Villanueva-Meyer, J., Chang, S., Clarke, J.L., Xu, D., Lupo, J.M., Larson, P.E., Vigneron, D.B., Li, Y., 2020a. Initial

Experience: Detection of Aberrat Metabolism with Hyperpolarized [1-13C]pyruvate metabolism in patients with GBM prior to resection. Neuro Oncol. 22, ii159.
Autry, A.W., Gordon, J.W., Chen, H.-Y., LaFontaine, M., Bok, R., Van Criekinge, M., Slater, J.B., Carvajal, L., Villanueva-Meyer, J.E., Chang, S.M., Clarke, J.L., Lupo, J. M., Xu, D., Larson, P.E.Z., Vigneron, D.B., Li, Y., 2020b. Characterization of serial hyperpolarized (13)C metabolic imaging in patients with glioma. Neuroimage Clin. 27, 102323.
Brender, J.R., Kishimoto, S., Merkle, H., Reed, G., Hurd, R.E., Chen, A.P., Ardenkjaer-Larsen, J.H., Munasinghe, J., Saito, K., Seki, T., Oshima, N., Yamamoto, K., Choyke, P.L., Mitchell, J., Krishna, M.C., 2019. Dynamic Imaging of Glucose and Lactate Metabolism by (13)C-MRS without Hyperpolarization. Sci. Rep. 9, 3410.
Chen, H.-Y., Autry, A.W., Brender, J.R., Kishimoto, S., Krishna, M.C., Vareth, M., Bok, R. A., Reed, G.D., Carvajal, L., Gordon, J.W., Criekinge, M., Korenchan, D.E., Chen, A. P., Xu, D., Li, Y., Chang, S.M., Kurhanewicz, J., Larson, P.E.Z., Vigneron, D.B., 2020. Tensor image enhancement and optimal multichannel receiver combination analyses for human hyperpolarized (13) C MRSI. Magn. Reson. Med. 84 (6), 3351–3365.
Crane, J.C., Gordon, J.W., Chen, H.Y., Autry, A.W., Li, Y., Olson, M.P., Kurhanewicz, J., Vigneron, D.B., Larson, P.E.Z., Xu, D., 2021. Hyperpolarized (13) C MRI data acquisition and analysis in prostate and brain at University of California, San Francisco. NMR Biomed. 34, e4280.
De Lathauwer, L., De Moor, B., Vandewalle, J., 2000. A multilinear singular value decomposition. SIAM J. Matrix Anal. Appl. 21 (4), 1253–1278.
Ellingson, B.M., Bendszus, M., Boxerman, J., Barboriak, D., Erickson, B.J., Smits, M., Nelson, S.J., Gerstner, E., Alexander, B., Goldmacher, G., Wick, W., Vogelbaum, M., Weller, M., Galanis, E., Kalpathy-Cramer, J., Shankar, L., Jacobs, P., Pope, W.B., Yang, D., Chung, C., Knopp, M.V., Cha, S., van den Bent, M.J., Chang, S., Yung, W.K., Cloughesy, T.F., Wen, P.Y., Gilbert, M.R., Jumpstarting Brain Tumor Drug Development Coalition Imaging Standardization Steering, C., 2015. Consensus recommendations for a standardized Brain Tumor Imaging Protocol in clinical trials. Neuro Oncol. 17, 1188–1198.
Golman, K., Zandt, R.I., Lerche, M., Pehrson, R., Ardenkjaer-Larsen, J.H., 2006. Metabolic imaging by hyperpolarized 13C magnetic resonance imaging for in vivo tumor diagnosis. Cancer Res 66, 10855-10860.
Gordon, J.W., Vigneron, D.B., Larson, P.E.Z., 2017. Development of a symmetric echo planar imaging framework for clinical translation of rapid dynamic hyperpolarized (13) C imaging. Magn. Reson. Med. 77 (2), 826–832.
Gordon, J.W., Chen, H.-Y., Autry, A., Park, I., Van Criekinge, M., Mammoli, D., Milshteyn, E., Bok, R., Xu, D., Li, Y., Aggarwal, R., Chang, S., Slater, J.B., Ferrone, M., Nelson, S., Kurhanewicz, J., Larson, P.E.Z., Vigneron, D.B., 2019. Translation of Carbon-13 EPI for hyperpolarized MR molecular imaging of prostate and brain cancer patients. Magn. Reson. Med. 81 (4), 2702–2709.
Gordon, J.W., Autry, A.W., Tang, S., Graham, J.Y., Bok, R.A., Zhu, X., Villanueva-Meyer, J.E., Li, Y., Ohilger, M.A., Abraham, M.R., Xu, D., Vigneron, D.B., Larson, P.E. Z., 2020. A variable resolution approach for improved acquisition of hyperpolarized (13) C metabolic MRI. Magn. Reson. Med. 84 (6), 2943–2952.
Gordon, J.W., Chen, H.-Y., Dwork, N., Tang, S., Larson, P.E.Z., 2021. Fast imaging for hyperpolarized MR metabolic imaging. J. Magn. Reson. Imaging 53 (3), 686–702.
Grist, J.T., McLean, M.A., Riemer, F., Schulte, R.F., Deen, S.S., Zaccagna, F., Woitek, R., Daniels, C.J., Kaggie, J.D., Matys, T., Patterson, I., Slough, R., Gill, A.B., Chhabra, A., Eichenberger, R., Laurent, M.C., Comment, A., Gillard, J.H., Coles, A.J., Tyler, D.J., Wilkinson, I., Basu, B., Lomas, D.J., Graves, M.J., Brindle, K.M., Gallagher, F.A., 2019. Quantifying normal human brain metabolism using hyperpolarized [1-(13)C] pyruvate and magnetic resonance imaging. Neuroimage 189, 171–179.
Grist, J.T., Miller, J.J., Zaccagna, F., McLean, M.A., Riemer, F., Matys, T., Tyler, D.J., Laustsen, C., Coles, A.J., Gallagher, F.A., 2020. Hyperpolarized (13)C MRI: A novel approach for probing cerebral metabolism in health and neurological disease. J. Cereb. Blood Flow Metab. 40 (6), 1137–1147.
Gudbjartsson, H., Patz, S., 1995. The Rician distribution of noisy MRI data. Magn. Reson. Med. 34 (6), 910–914.
Hatami, N., Sdika, M., Ratiney, H., 2018. Medical Image Computing and Computer Assisted Intervention In: Frangi, A.F., Schnabel, J.A., Davatzikos, C., Alberola-López, C., Fichtinger, G. (Eds.), MICCAI pp. 467-475.
Kim, Y., Chen, H.-Y., Autry, A.W., Villanueva-Meyer, J., Chang, S.M., Li, Y., Larson, P.E. Z., Brender, J.R., Krishna, M.C., Xu, D., Vigneron, D.B., Gordon, J.W., 2021. Denoising of hyperpolarized (13) C MR images of the human brain using patch-based higher-order singular value decomposition. Magn. Reson. Med. 86 (5), 2497–2511.
Lam, F., Li, Y., Peng, X.i., 2020. Constrained magnetic resonance spectroscopic imaging by learning nonlinear low-dimensional models. IEEE Trans. Med. Imaging 39 (3), 545–555.
Larson, P.E.Z., Chen, H.Y., Gordon, J.W., Korn, N., Maidens, J., Arcak, M., Tang, S., Criekinge, M., Carvajal, L., Mammoli, D., Bok, R., Aggarwal, R., Ferrone, M., Slater, J.B., Nelson, S.J., Kurhanewicz, J., Vigneron, D.B., 2018. Investigation of analysis methods for hyperpolarized 13C-pyruvate metabolic MRI in prostate cancer patients. NMR Biomed. 31, e3997.
Lee, P.M., Chen, H.-Y., Gordon, J.W., Zhu, Z., Larson, P.E.Z., Dwork, N., Van Criekinge, M., Carvajal, L., Ohliger, M.A., Wang, Z.J., Xu, D., Kurhanewicz, J., Bok, R.A., Aggarwal, R., Munster, P.N., Vigneron, D.B., 2021b. Specialized computational methods for denoising, B1 correction, and kinetic modeling in hyperpolarized (13) C MR EPSI studies of liver tumors. Magn. Reson. Med. 86 (5), 2402–2411.
Lee, C.Y., Soliman, H., Geraghty, B.J., Chen, A.P., Connelly, K.A., Endre, R., Perks, W.J., Heyn, C., Black, S.E., Cunningham, C.H., 2020. Lactate topography of the human brain using hyperpolarized (13)C-MRI. Neuroimage 204, 116202.
Lee, C.Y., Soliman, H., Bragagnolo, N.D., Sahgal, A., Geraghty, B.J., Chen, A.P., Endre, R., Perks, W.J., Detsky, J.S., Leung, E., Chan, M., Heyn, C., Cunningham, C. H., 2021a. Predicting response to radiotherapy of intracranial metastases with hyperpolarized [Formula: see text]C MRI. J. Neurooncol. 152, 551–557.
Lei, Y., Ji, B., Liu, T., Curran, W.J., Mao, H., Yang, X., 2021. Deep learning-based denoising for magnetic resonance spectroscopy signals. Medical Imaging 2021: Biomedical Applications in Molecular, Structural, and Functional Imaging.
Li, Y., Lupo, J.M., Polley, M.-Y., Crane, J.C., Bian, W., Cha, S., Chang, S., Nelson, S.J., 2011. Serial analysis of imaging parameters in patients with newly diagnosed glioblastoma multiforme. Neuro Oncol 13 (5), 546–557.
Li, Y., Vigneron, D.B., Xu, D., 2021. Current human brain applications and challenges of dynamic hyperpolarized carbon-13 labeled pyruvate MR metabolic imaging. Eur. J. Nucl. Med. Mol. Imaging 48 (13), 4225–4235.
Mammoli, D., Gordon, J., Autry, A., Larson, P.E.Z., Li, Y., Chen, H.-Y., Chung, B., Shin, P., Van Criekinge, M., Carvajal, L., Slater, J.B., Bok, R., Crane, J., Xu, D., Chang, S., Vigneron, D.B., 2020. Kinetic modeling of hyperpolarized carbon-13 pyruvate metabolism in the human brain. IEEE Trans. Med. Imaging 39 (2), 320–327.
Miloushev, V.Z., Granlund, K.L., Boltyanskiy, R., Lyashchenko, S.K., DeAngelis, L.M., Mellinghoff, I.K., Brennan, C.W., Tabar, V., Yang, T.J., Holodny, A.I., Sosa, R.E., Guo, Y.W., Chen, A.P., Tropp, J., Robb, F., Keshari, K.R., 2018. Metabolic Imaging of the Human Brain with Hyperpolarized (13)C Pyruvate Demonstrates (13)C Lactate Production in Brain Tumor Patients. Cancer Res 78, 3755-3760.
Park, I., Larson, P.E.Z., Gordon, J.W., Carvajal, L., Chen, H.-Y., Bok, R., Van Criekinge, M., Ferrone, M., Slater, J.B., Xu, D., Kurhanewicz, J., Vigneron, D.B., Chang, S., Nelson, S.J., 2018. Development of methods and feasibility of using hyperpolarized carbon-13 imaging data for evaluating brain metabolism in patient studies. Magn. Reson. Med. 80 (3), 864–873.
Pruessmann, K.P., Weiger, M., Bornert, P., Boesiger, P., 2001. Advances in sensitivity encoding with arbitrary k-space trajectories. Magn. Reson. Med. 46, 638–651.
Rajwade, A., Rangarajan, A., Banerjee, A., 2013. Image denoising using the higher order singular value decomposition. IEEE Trans. Pattern Anal. Mach. Intell. 35, 849–862.
Rolls, E.T., Huang, C.C., Lin, C.P., Feng, J., Joliot, M., 2020. Automated anatomical labelling atlas 3. Neuroimage 206, 116189.
Sanchez-Heredia, J.D., Olin, R.B., McLean, M.A., Laustsen, C., Hansen, A.E., Hanson, L. G., Ardenkjaer-Larsen, J.H., 2020. Multi-site benchmarking of clinical (13)C RF coils at 3T. J. Magn. Reson. 318, 106798.
Schroeder, M.A., Atherton, H.J., Ball, D.R., Cole, M.A., Heather, L.C., Griffin, J.L., Clarke, K., Radda, G.K., Tyler, D.J., 2009. Real-time assessment of Krebs cycle metabolism using hyperpolarized 13C magnetic resonance spectroscopy. FASEB J. 23, 2529–2538.
Wang, J., Wright, A.J., Hesketh, R.L., Hu, D.E., Brindle, K.M., 2018. A referenceless Nyquist ghost correction workflow for echo planar imaging of hyperpolarized [1-(13) C]pyruvate and [1-(13) C]lactate. NMR Biomed. 31.
Warburg, O., 1956. On the origin of cancer cells. Science 123, 309–314.
Zhang, Y., Brady, M., Smith, S., 2001. Segmentation of brain MR images through a hidden Markov random field model and the expectation-maximization algorithm. IEEE Trans. Med. Imaging 20, 45–57.
Zhang, X., Xu, Z., Jia, N., Yang, W., Feng, Q., Chen, W., Feng, Y., 2015. Denoising of 3D magnetic resonance images by using higher-order singular value decomposition. Med. Image Anal. 19, 75–86.
Zhang, X., Peng, J., Xu, M., Yang, W., Zhang, Z., Guo, H., Chen, W., Feng, Q., Wu, E.X., Feng, Y., 2017. Denoise diffusion-weighted images using higher-order singular value decomposition. Neuroimage 156, 128–145.
Zhu, Z., Zhu, X., Ohliger, M.A., Tang, S., Cao, P., Carvajal, L., Autry, A.W., Li, Y., Kurhanewicz, J., Chang, S., Aggarwal, R., Munster, P., Xu, D., Larson, P.E.Z., Vigneron, D.B., Gordon, J.W., 2019. Coil combination methods for multi-channel hyperpolarized (13)C imaging data from human studies. J. Magn. Reson. 301, 73–79.